

# On the Importance of Chemical Precision in Organic Electronics: Fullerene Intercalation in Perfectly Alternating Conjugated Polymers


Jochen Vanderspikken, Zhen Liu, Xiaocui Wu, Omar Beckers, Stefania Moro, Tyler James Quill, Quan Liu, Arwin Goossens, Adam Marks, Karrie Weaver, Mouna Hamid, Bart Goderis, Erik Nies, Vincent Lemaur, David Beljonne, Alberto Salleo, Laurence Lutsen, Koen Vandewal, Bruno Van Mele, Giovanni Costantini,\* Niko Van den Brande,\* and Wouter Maes\*

The true structure of alternating conjugated polymers—the state-of-the-art materials for many organic electronics—often deviates from the idealized picture. Homocoupling defects are in fact inherent to the widely used cross-coupling polymerization methods. Nevertheless, many polymers still perform excellently in the envisaged applications, which raises the question if one should really care about these imperfections. This article looks at the relevance of chemical precision (and lack thereof) in conjugated polymers covering the entire spectrum from the molecular scale, to the micro and mesostructure, up to the device level. The different types of polymerization errors for the alkoxylated variant of the benchmark (semi)crystalline polymer poly[2,5-bis(3-tetradecylthiophen-2-yl)thieno[3,2-*b*]thiophene (PBTtT)] are identified, visualized, and quantified and a general strategy to avoid homocoupling is introduced. Through a combination of experiments and supported by simulations, it is shown that these coupling defects hinder fullerene intercalation and limit device performance as compared to the homocoupling-free analog. This clearly demonstrates that structural defects do matter and should be generally avoided, in particular when the geometrical regularity of the polymer is essential. These insights likely go beyond the specific PBTtT derivatives studied here and are of general relevance for the wider organic electronics field.

## 1. Introduction

Due to the near-infinite number of possible structures and the large toolbox available to synthetic chemists, organic semiconductors (either polymers or small molecules) offer an unrivaled broad tunability for many materials and device parameters.<sup>[1]</sup> Semiconducting polymers are commonly used in optoelectronic devices, such as organic light-emitting diodes,<sup>[2]</sup> photovoltaics (OPVs),<sup>[3]</sup> transistors,<sup>[4]</sup> or photodetectors (OPDs),<sup>[5]</sup> and also applied in healthcare<sup>[6,7]</sup> and (photo)catalysis.<sup>[8]</sup> For many of these applications, low-bandgap push–pull (or donor–acceptor) type conjugated polymers are the state-of-the-art (photo)active materials. Push–pull copolymers are traditionally synthesized by operationally simple Pd-catalyzed (Stille, Suzuki, or direct arylation)<sup>[9,10]</sup> cross-coupling polymerizations to afford rigid backbones composed of alternating electron-rich and electron-deficient (hetero-aromatic) building blocks and they often yield

J. Vanderspikken, O. Beckers, Q. Liu, A. Goossens, L. Lutsen, K. Vandewal, W. Maes  
Institute for Materials Research (IMO)  
Hasselt University  
Agoralaan, Diepenbeek 3590, Belgium  
E-mail: wouter.maes@uhasselt.be

 The ORCID identification number(s) for the author(s) of this article can be found under <https://doi.org/10.1002/adfm.202309403>

© 2023 The Authors. Advanced Functional Materials published by Wiley-VCH GmbH. This is an open access article under the terms of the Creative Commons Attribution License, which permits use, distribution and reproduction in any medium, provided the original work is properly cited.

DOI: 10.1002/adfm.202309403

J. Vanderspikken, O. Beckers, Q. Liu, A. Goossens, L. Lutsen, K. Vandewal, W. Maes  
IMEC  
Associated Lab IMOMEC  
Wetenschapspark 1, Diepenbeek 3590, Belgium

J. Vanderspikken, O. Beckers, Q. Liu, A. Goossens, L. Lutsen, K. Vandewal, W. Maes  
Energyville  
Thorpark  
Genk 3600, Belgium

Z. Liu, B. Van Mele, N. Van den Brande  
Vrije Universiteit Brussel  
Physical Chemistry and Polymer Science  
Pleinlaan 2, Brussels 1050, Belgium  
E-mail: niko.van.den.brande@vub.be

excellent device results. Nevertheless, these polymerization reactions do suffer from a lack of control over the exact polymer composition and end groups.<sup>[11]</sup>

Over the last decade, it has been shown that homocoupling defects (i.e., monomer units coupling to themselves rather than to the complementary functionalized comonomer) occur quite readily during cross-coupling polymerizations.<sup>[10,12–16]</sup> This has been attributed to catalyst aging and/or the presence of oxidative species but seems hard to avoid completely and is likely among the various causes (next to molar mass and dispersity) of the well-known batch-to-batch variations of push–pull conjugated polymers.<sup>[12–14,17]</sup> In some cases, homocoupling was shown to result in compromised device (notably solar cell) efficiencies, whereas other polymers seem rather forgiving in terms of defect tolerance. This raises the question if a perfectly alternating structure is of crucial importance or merely of academic interest.

To judge if homocoupling defects are indeed relevant, it is essential to precisely identify their nature and quantity in order to understand the molecular origin of their (possibly deleterious) effects. Moreover, synthetic methods should be developed to avoid all coupling errors (if only) to ultimately permit a correct comparison and analysis. So far, however, it has been difficult to control and even analyze the amount of homocouplings.<sup>[18]</sup> Occasionally, quantification via NMR is done but this is far from simple and, at times, even impossible for some of the most relevant systems because of severe peak broadening.<sup>[17,18]</sup> Additionally, the rather low sensitivity of NMR does not allow to detect ppm-scale defect levels which might already affect device performance. Matrix-assisted laser desorption-ionization–time of flight mass spectrometry (MALDI-ToF MS) gives an idea of the various species present, but quantification is troublesome and the connectivity of the constituting monomers remains unknown. Other methods (e.g., absorption spectroscopy) only provide indirect evidence of the occurrence of defects.<sup>[12,14]</sup> Only recently, molecular

scale imaging of conjugated polymers by ultrahigh vacuum scanning tunneling microscopy (UHV-STM) has shown the ability to identify and quantify polymerization defects,<sup>[18,19]</sup> but a systematic study has been lacking so far.

In our search for a suitable benchmark polymer to perform an in-depth study on the occurrence and relevance of homocoupling defects, we turned to poly[2,5-bis(3-tetradecylthiophen-2-yl)thieno[3,2-*b*]thiophene (PBTTT). Although not being a true push–pull conjugated polymer, PBTTT is commonly made via Stille cross-coupling<sup>[20]</sup> and shows one of the highest degrees of (semi)crystallinity, rendering it a benchmark material in the field. Its (semi)crystalline nature allows the use of X-ray scattering techniques to probe the molecular organization, microstructure, crystallite size, disorder, etc.,<sup>[21–23]</sup> and how these are affected by the molecular structure. Additionally, PBTTT is one of the few polymers that allow intercalation of fullerene acceptors between the side chains, thereby forming a thermodynamically stable co-crystal.<sup>[24,25]</sup> The molecularly mixed PBTTT:PC<sub>61</sub>BM ([6,6]-phenyl-C<sub>61</sub>-butyric acid methyl ester) blend shows intermolecular charge-transfer (CT) absorption in the sub-gap spectral region, the strength of which correlates with the donor:acceptor interfacial area.<sup>[26]</sup> The properties of the CT states determine the photovoltage when used in OPVs<sup>[27,28]</sup> and the long-wavelength CT absorption can be used for wavelength-selective near-infrared (NIR) OPDs in a resonance optical cavity device architecture.<sup>[29,30]</sup> In previous work, this CT absorption was red-shifted (i.e., the polymer:PC<sub>61</sub>BM interfacial energy gap was reduced) by exchanging the alkyl side chains with alkoxy variants.<sup>[31]</sup> However, as compared to PBTTT, the fully alkoxyated PBTTT-(OR)<sub>2</sub> polymer showed a significantly less intense CT absorption when mixed with PC<sub>61</sub>BM. This was tentatively attributed to diminished (or even absent) fullerene intercalation, possibly due to structural defects. Thus, the PBTTT-(OR)<sub>2</sub> polymer is an ideal candidate for further studies on the effect of polymerization defects.

In the present work, PBTTT-(OR)<sub>2</sub> is synthesized by the traditional Stille procedure, as well as by an alternative oxidative homopolymerization strategy to circumvent homocoupling. Through high-resolution STM, we precisely identify the nature of the polymerization errors in Stille-synthesized PBTTT-(OR)<sub>2</sub> and quantify the amount of homocoupling. Moreover, STM confirms the complete absence of homocoupling defects for the alternative synthetic approach. The two polymer batches are then compared as pristine materials and in mixtures with PC<sub>61</sub>BM by a complementary combination of rapid heat–cool differential scanning calorimetry (RHC) and temperature-resolved synchrotron X-ray diffraction (XRD), supported by molecular dynamics (MD) simulations and juxtaposed to benchmark PBTTT.<sup>[20,22,25,32]</sup> This analysis shows that homocoupling is detrimental for geometrical rather than electronic reasons, as it hinders fullerene intercalation in Stille-PBTTT-(OR)<sub>2</sub>, whereas intercalation is recovered for the homocoupling-free polymer. This is also reflected at the (OPD) device level, where enhanced CT absorption is observed for the mixture of oxidatively synthesized PBTTT and PC<sub>61</sub>BM, whereas it is significantly reduced for the (homocoupling defective) Stille analog. Our study hence tackles the question of the relevance of chemical precision in conjugated polymers in a comprehensive way, covering the entire spectrum; we identify the different defects at the molecular scale, analyze their effect on the

X. Wu  
Department of Chemistry  
University of Warwick  
Gibbet Hill Road, Coventry CV4 7AL, UK

S. Moro, G. Costantini  
School of Chemistry  
University of Birmingham  
Edgbaston, Birmingham B15 2TT, UK  
E-mail: g.costantini@bham.ac.uk

T. J. Quill, A. Marks, A. Salleo  
Department of Materials Science and Engineering  
Stanford University  
Stanford, CA 94305, USA

K. Weaver  
Department of Earth System Science  
Stanford University  
Stanford, CA 94305, USA

M. Hamid, B. Goderis, E. Nies  
KU Leuven  
Polymer Chemistry and Materials Division  
Celestijnenlaan 200F, Heverlee 3001, Belgium

V. Lemaur, D. Beljonne  
Laboratory for Chemistry of Novel Materials  
Materials Research Institute  
University of Mons (UMONS)  
20 Place du Parc, Mons B-7000, Belgium

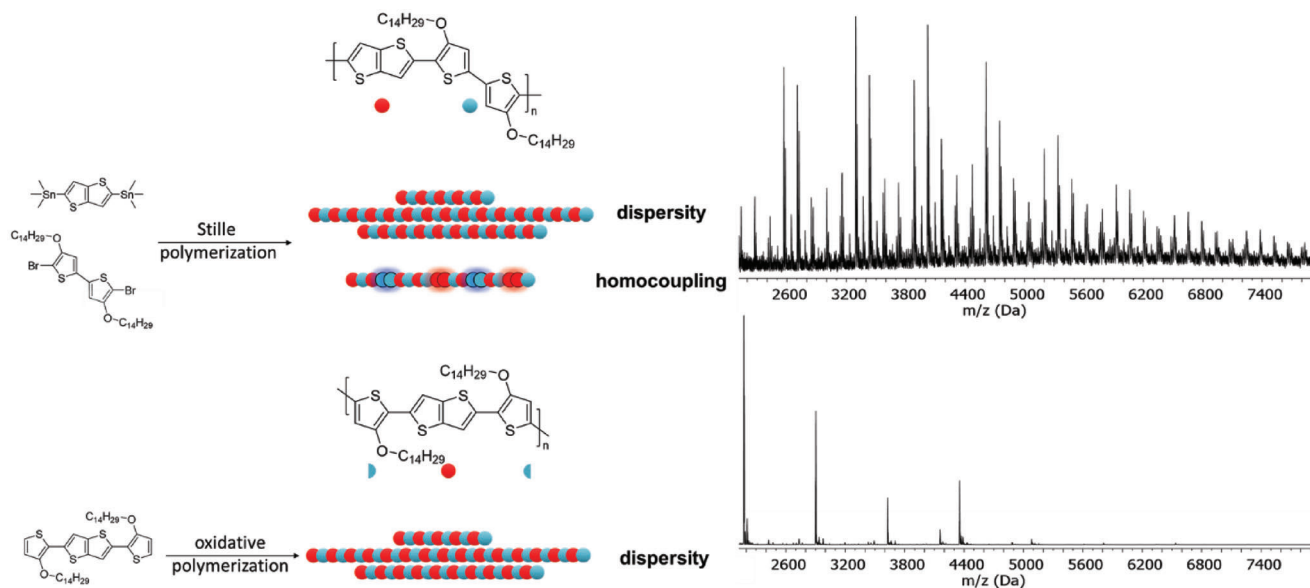


**Figure 1.** Conventional (top) and alternative oxidative homopolymerization approach (bottom) to synthesize PBTTT-(OR)<sub>2</sub>. The MALDI-ToF mass spectra at the right show that the former results in a significantly larger number of different species, among which there are a lot of homocoupled structures, whereas the latter affords a material much closer to the ideal structure, with a drastically reduced number of different species. See Figure S2, Supporting Information, for large-scale images of the MALDI-ToF MS spectra.

micro and mesostructure of the pure polymers and in mixtures with fullerenes, and ascertain that they are deleterious up to the device level. Moreover, a generic synthetic strategy to avoid homocoupling errors is introduced. Finally, the generality of these findings and their relevance for the wider field of organic electronics are discussed.

## 2. Results and Discussion

### 2.1. Polymer Synthesis and Structural Analysis

**Figure 1** (top left) shows a schematic overview of the conventional Stille approach to synthesize PBTTT-(OR)<sub>2</sub>. Apart from the correctly coupled polymer chains with various lengths, matching to the expected structure of alternating thieno[3,2-*b*]thiophene (TT) and bithiophene (BT) units, this route produces a significant fraction of homocouplings, as identified by MALDI-ToF MS (Figure 1, top right). These structurally defected species are virtually inseparable from the fraction of polymers that correspond to correct sequences. A detailed assignment of all species identified in the Stille polymer by MALDI-ToF MS can be found in Figure S3, Supporting Information, which suggests a large amount of TT homocoupling.

We, therefore, employed an alternative, less common synthesis route (Figure 1, bottom left), wherein the monomer 2,5-bis[3-(tetradecyloxy)thiophen-2-yl]thieno[3,2-*b*]thiophene was homopolymerized in an oxidative manner using iron(III) chloride (FeCl<sub>3</sub>), based on reported conditions for poly-3-hexylthiophene and previously applied for some other polythiophenes as well.<sup>[33–35]</sup> The advantage of this strategy is that the required cross-coupling now occurs at the monomer stage, where it is still possible to discard side products. Details on the synthesis and characterization can be found in the Supporting Information.

With the alternative homopolymerization approach, we almost exclusively observed MS signals corresponding to multiples of the mass of the repeating unit (Figure 1, bottom right), resulting in much cleaner spectra, indeed suggesting a much better-defined polymer structure with little to no defects. <sup>1</sup>H NMR spectroscopy (Figure S4, Supporting Information) still displays broad signals for homocoupling-free PBTTT-(OR)<sub>2</sub> due to polymer aggregation and hence does not allow detailed comparison. X-ray photoelectron spectroscopy (XPS) was also performed on the two polymer samples. In the case of significant TT homocoupling, as suggested by MALDI-ToF MS, one would expect to see a clear offset in the ratio of sulfur, oxygen, and carbon with respect to the relative stoichiometry of the ideal polymer. However, the observed atomic ratios are nearly identical for both synthetic approaches (Figure S5, Supporting Information). We, therefore, hypothesize that MALDI-ToF MS grossly overestimates the amount of TT homocoupling. It was noticed before that homocoupling of the nucleophilic Stille monomer shows up more strongly in MALDI-ToF mass spectra,<sup>[36]</sup> which might be attributed to the electron-accepting nature of the matrix used<sup>[15,36,37]</sup> (see Experimental Section) and indicates that statements on conjugated polymer structures based on MALDI-ToF MS have to be made with great caution. The smaller mass of TT as compared to the alkoxyated BT monomer might play a role here as well, as signal intensity decreases with molar mass in MALDI-ToF MS and the spectra hence preferentially show the low molar mass species in a conjugated polymer distribution.

STM analysis (**Figure 2**; larger-scale images in Figure S6, Supporting Information) provides a definitive answer on the actual structure of the oxidatively synthesized polymer and the homocoupling distribution in Stille PBTTT-(OR)<sub>2</sub>. These measurements were performed in situ on polymers transferred onto single crystalline (111) gold samples by electrospray deposition in

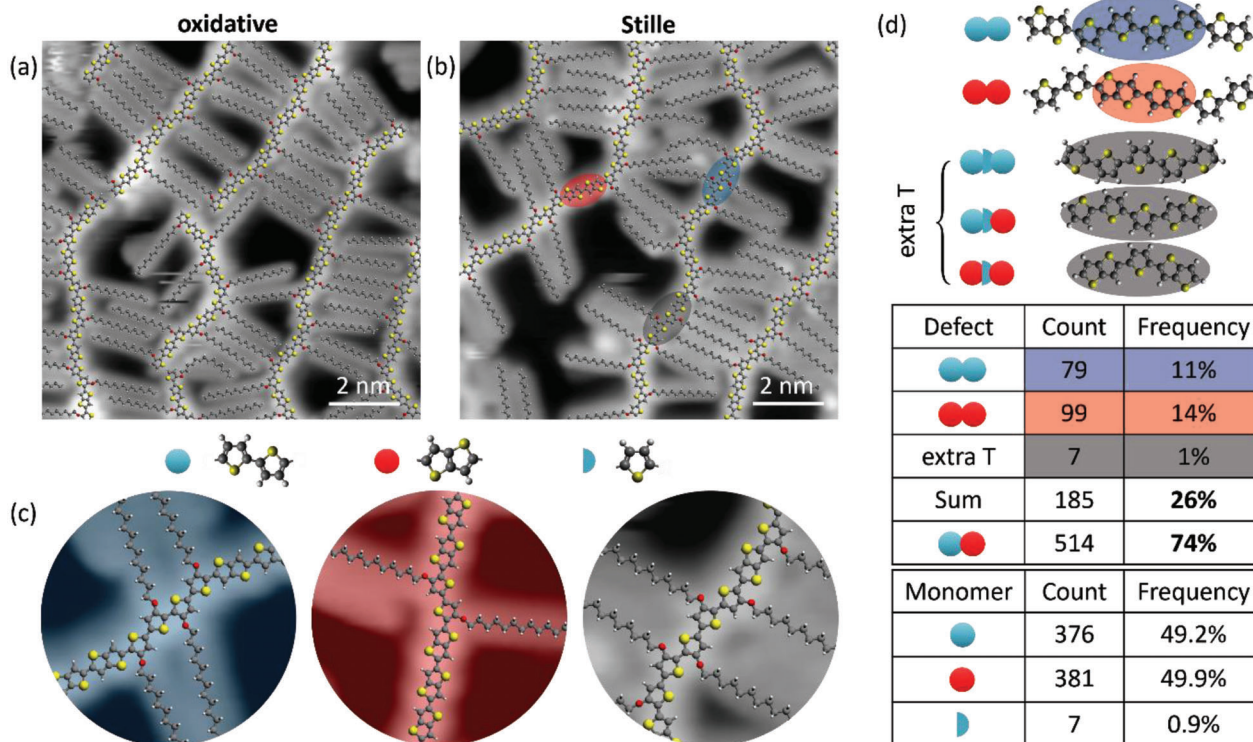


**Figure 2.** High-resolution STM images of a) oxidatively synthesized ( $10\text{ nm} \times 10\text{ nm}$ ,  $V = 1.3\text{ V}$ ,  $I = 58\text{ pA}$ ) and b) Stille ( $10\text{ nm} \times 10\text{ nm}$ ,  $V = 484\text{ mV}$ ,  $I = 78\text{ pA}$ ) PBTTT-(OR)<sub>2</sub>. Geometry-optimized molecular models are overlaid on the STM images. The BT and TT homocouplings are marked by blue and red ovals, respectively. A very small fraction of extra single T units (gray oval) is observed as well. c) Close-up images and d) molecular models (without side chains) and corresponding quantification of the BT and TT homocouplings and extra T defect in the Stille-synthesized polymer. No defects were observed in the oxidative polymer. Importantly, the ratio of BT and TT monomers appears almost identical for both polymers.

UHV. The high-resolution imaging of the polymers and their fitting by geometry-optimized molecular models unequivocally grants access to their precise sequence at the sub-monomer scale.<sup>[18,19,38,39]</sup> The analysis of the oxidatively synthesized polymer shows no signs of homocoupling, confirming its structural perfection (Figure 2a). On the other hand, Stille PBTTT-(OR)<sub>2</sub> (Figure 2b) displays a large number of homocouplings. Close-up images of the defects are shown in Figure 2c, and their molecular models and quantification are presented in Figure 2d. Next to TT homocoupling (Figure 2c left, 14%), also BT homocoupling (Figure 2c middle, 11%) was detected in significant amounts, giving a ratio between the constituting monomers of 1:1, in good agreement with the XPS results. It is worthwhile noting that up to 5 TT monomers and up to 4 BT monomers were seen in succession, suggesting clear correlation effects between homocoupling defects. A very small fraction (less than 1%) of single thiophene (T) units were also observed between TT and/or BT monomers (extra T defect as shown in Figure 2c right and by models in Figure 2d), likely resulting from minor monomer impurities. Although  $\beta$  rather than  $\alpha$ -thiophene coupling can potentially occur when using an oxidative synthesis protocol, extensive amounts of beta coupling would have been picked up by STM. As this was not seen, we can cautiously conclude that  $\beta$ -couplings, if any, are present to a minor extent. Further details on the acquisition of the STM images, homocoupling content analysis, and mass distribution determination are provided in the Supporting Information.

Despite their clearly different structure, the UV-vis-NIR absorption traces (Figure S7, Supporting Information) and the frontier orbital energy levels as estimated by cyclic voltammetry (Figure S8, Supporting Information) are similar for the two PBTTT-(OR)<sub>2</sub> samples. This illustrates that the structural defects, in this particular case and even when present in significant numbers, do not strongly affect the electronic properties of the polymer. Even though FeCl<sub>3</sub> is a well-known *p*-type dopant, no polaronic features are present in the absorption spectra nor in the oxidation curves for the newly synthesized polymer.<sup>[40]</sup> Inductively coupled plasma-mass spectrometry (ICP-MS) analysis was performed to evaluate the presence of residual Fe species for the oxidative synthesis route. Somewhat surprisingly, the oxidative and Stille PBTTT-(OR)<sub>2</sub> contain comparable amounts of Fe (562 and 449 ppm, respectively). Similar Fe levels have also been observed in other Stille-synthesized conjugated polymers but its exact origin still needs to be unraveled.

## 2.2. Morphological Transitions of the Pristine Polymers and the Polymer:PC<sub>61</sub>BM Mixtures

Next, we analyzed the impact of the presence of homocoupling defects on the temperature-dependent polymer morphology and fullerene intercalation. Figure 3 shows the RHC thermograms of the two PBTTT-(OR)<sub>2</sub> polymer batches in comparison with

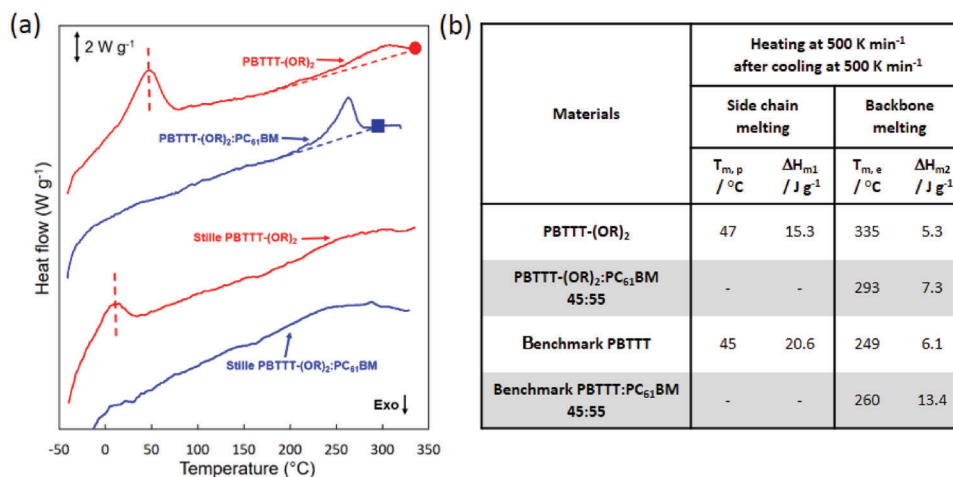


**Figure 3.** a) RHC heating at 500 K min<sup>-1</sup> after cooling at 500 K min<sup>-1</sup> from 335 °C for oxidative (upper) and Stille PBTTT-(OR)<sub>2</sub> (lower, adapted from ref.<sup>[31]</sup>), in pure polymer form (red curves) and mixed with PC<sub>61</sub>BM in a 45:55 w/w% ratio (blue curves). Curves are vertically shifted for clarity. b) Peak temperature of side chain melting ( $T_{m,p}$ ), enthalpy of side chain melting ( $\Delta H_{m1}$ ), endset temperature of backbone melting of the polymer or co-crystals ( $T_{m,e}$ ), and enthalpy of backbone melting ( $\Delta H_{m2}$ ).

their respective mixtures with PC<sub>61</sub>BM in a 45:55 w/w% ratio, that is, close to the 1:1 molar ratio of the polymer repeating units and PC<sub>61</sub>BM. MD simulations reveal that PBTTT-(OR)<sub>2</sub> is arranged in lamellar stacks in which molecular backbone layers alternate with layers from interdigitating side chains (Figure 4), closely resembling the regular PBTTT structure (Figure S9, Supporting Information). At sufficiently low temperatures, the stretched side chains (in all all-*trans* configuration) are in a crystalline state, the selective melting of which is referred to as “side chain melting”.<sup>[24]</sup> The layer assembly converts into a homogeneous liquid only at a much higher temperature, the so-called

“backbone melting” temperature. The alkoxy side chain melting peak,  $T_{m,p}$ , is indicated with a vertical dashed line in Figure 3, whereas the endset temperature for backbone melting,  $T_{m,e}$ , is indicated by a red-filled circle for the pure polymer and a blue-filled square for the PBTTT-(OR)<sub>2</sub>:PC<sub>61</sub>BM mixture, respectively.

In Figure 3b, the values of  $T_{m,p}$  and  $T_{m,e}$  for the oxidatively synthesized PBTTT-(OR)<sub>2</sub> polymer are compared to the corresponding values of the benchmark (Stille synthesized; Table S1, Supporting Information) PBTTT, for which MALDI-ToF MS measurements (Figure S3, Supporting Information) showed few homocoupling defects. While the  $T_{m,e}$  value is larger for

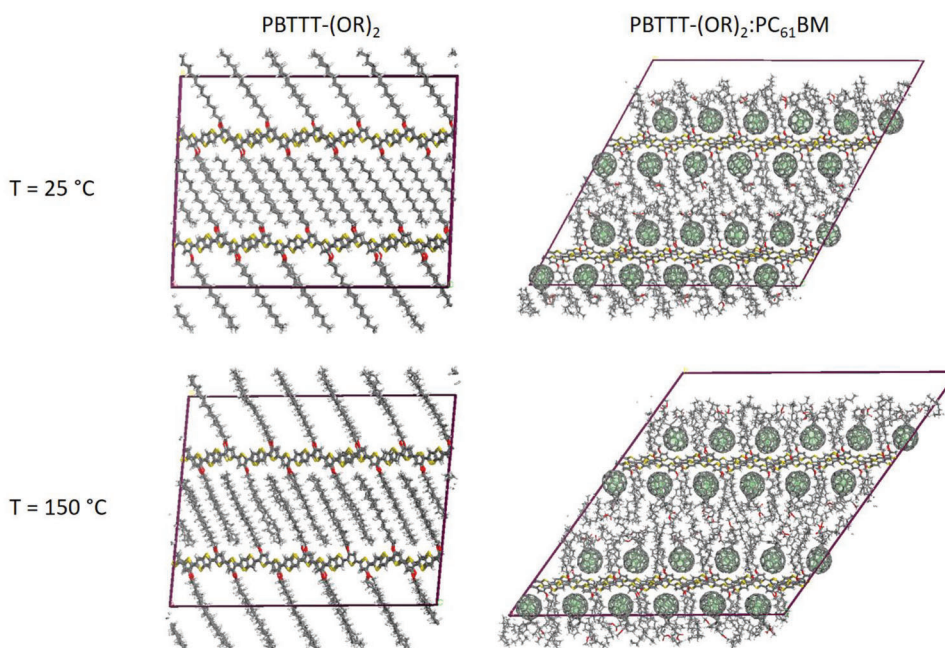


**Figure 4.** Representation of the simulated organizations of neat PBTTT-(OR)<sub>2</sub> (left) and PBTTT-(OR)<sub>2</sub> mixed with PC<sub>61</sub>BM (right) at 25 and 150 °C (last snapshots of 1 ns-long molecular dynamics). Size indications are provided in Figure 5b.

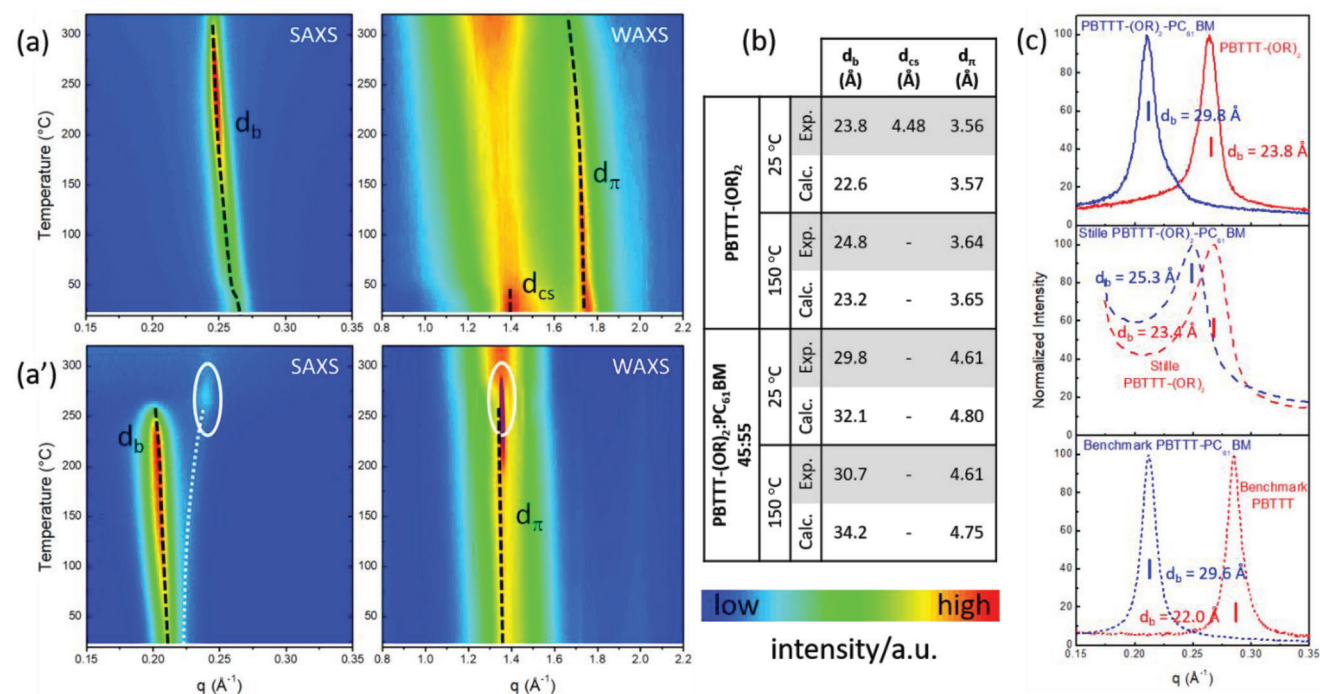


**Figure 5.** Temperature-resolved synchrotron SAXS and WAXS patterns as a function of  $q$  for a) oxidative PBTTT-(OR)<sub>2</sub> and a') its co-crystal (i.e., oxidative PBTTT-(OR)<sub>2</sub> mixed with PC<sub>61</sub>BM in a 45:55 w/w% ratio) upon heating at 50 K min<sup>-1</sup> from room temperature to 320 °C after slow cooling at 20 K min<sup>-1</sup> from 335 to -50 °C. The colors are indicative of the relative intensity of the diffraction patterns. The black dashed lines in (a) and (a') highlight the tracks of the reflections associated with the lamellar spacing or backbone-to-backbone separation distance along the layer stacking ( $d_b$ ), the side chain packing in the crystalline state ( $d_{cs}$ ), and the  $\pi$ - $\pi$  stacking distance ( $d_\pi$ ). The dotted white line in (a') highlights the track of a weak reflection, tentatively associated with PBTTT-(OR)<sub>2</sub> stacks that are only partially intercalated with PC<sub>61</sub>BM. The circled high-temperature reflections in (a') relate to pure PBTTT-(OR)<sub>2</sub> (SAXS) and pure PC<sub>61</sub>BM (WAXS) as a result of incongruent melting of the co-crystal. The intensity of the PC<sub>61</sub>BM reflection is very high and falls outside the color scale. It is therefore colored in purple. b) Values for  $d_b$ ,  $d_{cs}$ , and  $d_\pi$  at 25 and 150 °C for oxidatively polymerized PBTTT-(OR)<sub>2</sub> and PBTTT-(OR)<sub>2</sub>:PC<sub>61</sub>BM in a 45:55 w/w% ratio, obtained from the SAXS and WAXS experiments (exp.) and from simulations (calc.), of which snapshots are shown in Figure 4. c) SAXS patterns at room temperature for the polymers in pure form (red) and mixed with PC<sub>61</sub>BM (blue) in a 45:55 w/w% ratio for oxidatively polymerized PBTTT-(OR)<sub>2</sub> (upper panel, full lines) and benchmark PBTTT (lower panel, dotted lines), and in a 50:50 w/w% ratio for Stille PBTTT-(OR)<sub>2</sub> (middle panel, dashed lines; adapted from ref.[31] and based on measurements with a laboratory Bruker D8 Discover setup). The  $d$ -spacings corresponding to the  $q$ -values of the peak maxima (marked with short vertical lines) are indicated.

PBTTT-(OR)<sub>2</sub> than for PBTTT, the opposite is true for the corresponding melting enthalpies ( $\Delta H_{m2}$ ). Given the relation  $T_{m,e} = \Delta H_{m2} / \Delta S_{m2}$ , this implies a lower entropy gain ( $\Delta S_{m2}$ ) during the backbone melting transition for PBTTT-(OR)<sub>2</sub> than for PBTTT. Assuming comparable entropies of the random melt state for both polymers, it follows that the entropy of the lamellar stacks (in which the side chains are already molten) for PBTTT-(OR)<sub>2</sub> is higher than for PBTTT. This higher entropy is likely associated with the more flexible alkoxy side chains. These more dynamic alkoxy side chains also prevent the formation of a liquid crystalline state at temperatures between the crystalline and liquid side chain states, which is known to exist in PBTTT.<sup>[20]</sup> Indeed, in contrast to PBTTT, a liquid crystalline to liquid transition of the side chains is not seen for PBTTT-(OR)<sub>2</sub>, irrespective of the preceding cooling rate (see Figure S10, Supporting Information).

In Figure 3a, a new melting transition is observed for oxidatively polymerized PBTTT-(OR)<sub>2</sub> mixed with PC<sub>61</sub>BM in a 45:55 w/w% ratio, which is completely absent for the Stille polymer, corresponding to the intercalated co-crystal of PC<sub>61</sub>BM with PBTTT-(OR)<sub>2</sub>. In this case, no side chain melting nor melting of pure PC<sub>61</sub>BM crystals is seen. The PBTTT-(OR)<sub>2</sub> co-crystal melts at a lower temperature (expressed in terms of  $T_{m,e}$ ) than

pure PBTTT-(OR)<sub>2</sub>, while the  $T_{m,e}$  of the co-crystal of benchmark PBTTT is higher than that of pure PBTTT.<sup>[31]</sup> In each case, the  $\Delta H_{m2}$  of the co-crystals is higher than that of the corresponding pure polymers (see Figure 3b), pointing again at entropy effects.

Further evidence for the interpretation of the RHC measurements is present in the T-resolved small angle (SAXS) and wide angle (WAXS) X-ray scattering data of Figure 5. Three prominent reflections are highlighted in the SAXS and WAXS plots of oxidative PBTTT-(OR)<sub>2</sub> using dashed black lines (Figure 5a). The  $d_b$  (i.e., backbone-to-backbone) labeled reflection in SAXS corresponds to the (first order) reflection of the lamellar spacing. The corresponding  $d$ -spacings ( $d = 2\pi/q$ ) at 25 and 150 °C are shown in Figure 5b and compared with values calculated from the MD simulated structures (Figure 4). Upon heating, this reflection shifts to lower  $q$ -values, indicating an expanding lamellar spacing. Up to 220 °C, the intensity of this reflection grows, likely as a result of an increasing electron density difference (contrast) between the molecular backbone and side chain layers induced by thermal expansion. Beyond 220 °C, the intensity of this SAXS reflection collapses due to dominating backbone melting (stack dissolution) but does not reach a zero value at 320 °C, the highest temperature in this experiment. Extrapolating the evolution of

this reflection's intensity to higher temperatures forecasts a zero intensity at  $\approx 335$  °C, that is, the  $T_{m,e}$  value determined by RHC (Figure 3b).

Identification of the side chain aggregation state of oxidative PBTTT-(OR)<sub>2</sub> follows from the WAXS patterns (Figure 5a). The reflection at approximately  $q = 1.40 \text{ \AA}^{-1}$  (labeled  $d_{cs}$ ) is related to the crystalline side chain packing at 25 °C ( $d_{cs} \approx 4.48 \text{ \AA}$ ) and converts to a broad halo upon heating above 50 °C, indicating a transition of the side chains to the liquid state. The WAXS patterns also contain a reflection (labeled  $d_{\pi}$ ) related to the  $\pi$ - $\pi$  stacking distance of neighboring polymer backbones. For the benchmark PBTTT (Figure S11, Supporting Information), the latter reflection at 25 °C peaks at about  $q = 1.74 \text{ \AA}^{-1}$ , which corresponds to a  $d_{\pi}$  value of 3.60 Å and which compares well to earlier reported values.<sup>[41]</sup> The  $d_{\pi}$  value for PBTTT-(OR)<sub>2</sub> is somewhat shorter (3.56 Å), in line with the values derived from the simulations (Figure 5b). At the RHC onset of backbone melting ( $\approx 180$  °C, Figure 3b), the intensity of this  $d_{\pi}$  reflection starts diminishing and ultimately declines simultaneously with the  $d_b$  reflection. Scattering of the melted material adds to the broad amorphous halo of the homogeneous liquid state.

Figure 5a' shows the T-resolved SAXS and WAXS patterns for the co-crystal of oxidative PBTTT-(OR)<sub>2</sub> mixed with PC<sub>61</sub>BM in a 45:55 w/w% ratio. The reflection due to the co-crystal lamellar spacing is found at a markedly lower  $q$ -value, demonstrating an increase of 6 Å in the backbone-to-backbone separation with respect to pure PBTTT-(OR)<sub>2</sub> (for comparison,  $d_b$  increases by 7.6 Å when the benchmark PBTTT is mixed with PC<sub>61</sub>BM in the same ratio; see Figure S11b, Supporting Information). Remarkably, the co-crystal  $d_b$ -spacings for both oxidatively synthesized PBTTT-(OR)<sub>2</sub> and benchmark PBTTT are very close to 30 Å. The clear difference in the pure polymers is completely wiped out by the successful intercalation with PC<sub>61</sub>BM. Limited or partial intercalation for Stille PBTTT-(OR)<sub>2</sub> is evidenced by the absence of a SAXS peak at the typical  $q$ -values for "perfectly intercalated" co-crystals and a shift to higher  $q$ -values close to the pure polymer (Figure 5c). Lamellar ordering of pure oxidative PBTTT-(OR)<sub>2</sub> is not observed in the SAXS patterns of the 45:55 w/w% mixture, except at very high temperatures as a result of incongruent melting (Figure 5a'). Because of the PC<sub>61</sub>BM intercalation, the side chains cannot crystallize and the associated  $d_{cs}$  WAXS reflection is therefore absent (Figure 5a'). The  $d_{\pi}$ -spacing in the co-crystals is increased by  $\approx 1$  Å compared to the pure polymers, again in agreement with the calculated  $d_{\pi}$  values from the MD simulations (Figure 5b and Figure S11b, Supporting Information).<sup>[25,41]</sup>

Since semiconducting polymers are applied as thin films in optoelectronic devices, grazing-incidence wide-angle X-ray scattering (GIWAXS) analysis was also performed on films of the pristine PBTTT-(OR)<sub>2</sub> polymers and their mixtures with PC<sub>61</sub>BM (in the 20:80 w/w% ratio as used in devices). GIWAXS analysis of the oxidative and Stille-synthesized polymers shows very little difference (Figure S12, Supporting Information), apart from a slightly shorter  $\pi$ - $\pi$  stacking distance for oxidatively synthesized PBTTT-(OR)<sub>2</sub>. For the PC<sub>61</sub>BM mixtures (Figure S13, Supporting Information), the most striking observation is the absence of a co-crystal lamellar stacking peak for Stille PBTTT-(OR)<sub>2</sub>. The homocoupling-free material, on the other hand, shows a clear co-crystal peak. These observations are fully in line with the RHC and powder XRD results.

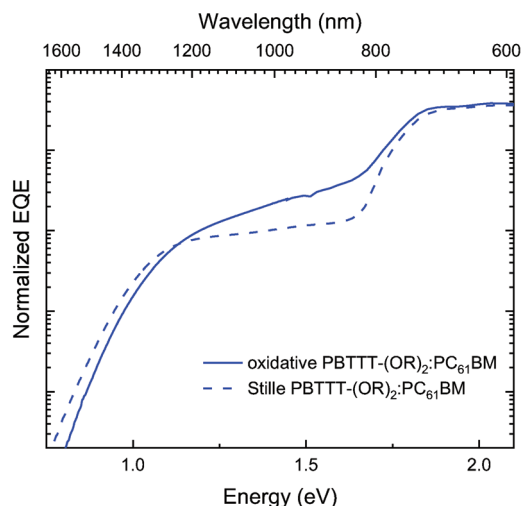


**Figure 6.** Normalized EQE spectra for OPD devices composed of oxidatively synthesized PBTTT-(OR)<sub>2</sub> mixed with PC<sub>61</sub>BM (20:80 w/w%).

### 2.3. Charge-Transfer Absorption

From the above, it can be concluded that the oxidatively synthesized PBTTT-(OR)<sub>2</sub> shows marked differences with respect to the (homocoupling defective) Stille polymer, such as a clearer side chain and backbone melting, and most strikingly, an obvious co-crystal melting when mixed with PC<sub>61</sub>BM (Figure 3a), which is absent for the Stille polymer. The recovery of the fullerene intercalation features for homocoupling-free PBTTT-(OR)<sub>2</sub> results in an increased interfacial contact, which is of relevance for organic solar cells and (cavity-based) OPDs,<sup>[29,31]</sup> where the performance is strongly affected by donor-acceptor intermolecular interactions and interfacial contact area. This is probed by external quantum efficiency (EQE) spectra, measured using Fourier-transform photocurrent spectroscopy (FTPS), which has the required sensitivity to probe sub-gap absorption by CT states.<sup>[28]</sup> Figure 6 shows the normalized EQE spectra on a logarithmic scale for prototype PBTTT-(OR)<sub>2</sub>:PC<sub>61</sub>BM (20:80 w/w%) photodiodes, displaying the weak CT absorption bands in the NIR. Stille PBTTT-(OR)<sub>2</sub> affords 2–3 times less CT absorption than oxidative PBTTT-(OR)<sub>2</sub>. This illustrates the clear impact of homocoupling on donor-acceptor intermolecular interactions, important for the application of these molecular mixtures in devices. On the other hand, charge (hole) transport—as probed by organic field-effect transistor (OFET) measurements—appears to be rather resilient to homocoupling defects (see Supporting Information for details; Figure S14, Supporting Information), even though further dedicated analysis on polymers of similar molar mass is needed to make definite statements on this matter.

## 3. Conclusions

In the field of organic electronics, mixtures of organic/polymer compounds are often used to introduce new functionalities that do not exist in the individual components, thereby realizing unprecedented material and device properties.<sup>[42]</sup> A notable example is the combination of the (semi)crystalline polymer PBTTT

and the methanofullerene PC<sub>61</sub>BM. Intercalation of the fullerene bucky balls in between the polymer side chains gives rise to a “molecular compound” with distinct features. This nanoscale mixing of the two components has for instance been used to achieve enhanced detectivities in cavity photodetectors.<sup>[29,31]</sup> However, the beneficial properties of organic semiconductor mixtures can be masked by the presence of defects in one (or more) of the materials, as indicated in this work. As such, cooperative actions of the constituting molecules might simply be overlooked, many valuable materials (combinations) might be discarded, and new insights in structure-mixture-performance relations could be lost. It is hence imperative to achieve a precise characterization of the real structures of the pristine materials and to ensure that these correspond to those expected.

For push–pull alternating copolymers, it is known that homocoupling defects can occur during cross-coupling polymerizations. Although, in most cases, this is neglected as the final devices work satisfactorily, this might not be the best way to approach this conundrum. A few dedicated studies have clearly shown a direct and negative impact of homocoupling on solar cell device performance.<sup>[12–14]</sup> Besides, some homocoupling-free alternating conjugated polymers, synthesized via novel strategies, were shown to afford higher field-effect mobilities than the analogous materials that do contain structural defects.<sup>[17,43]</sup> Nevertheless, the generality of these effects has not been demonstrated and is complicated by the system-dependent ratio of homocoupling and its varying effect on electronic and/or morphological (blend) properties. As such, the relevance for the wider field is still under debate. Although structural purification will not always automatically lead to enhanced (device) performance—for example, in specific cases, some structural irregularity might even be welcome to avoid over-aggregation, enhance miscibility, etc.—true structure-property insights can only be established and applied to foster further progress if one is fully aware of the structural reality and the effects of imperfections.

By analyzing the PBTTT-(OR)<sub>2</sub> model system, we provide a clear example where the true potential of organic semiconductor mixtures can only be achieved if homocoupling mistakes are avoided. A multiscale strategy is adopted, gradually moving from the molecular structure of single polymer chains to the micro and mesostructure of polymer:fullerene mixtures, all the way up the device level. We introduce a model synthetic approach to discard homocoupling in alternating conjugated polymers by constructing a monomer containing both the envisaged building blocks and then subjecting it to a homopolymerization reaction. This is a conceptually simple, elegant, and effective strategy, although (for symmetry reasons) being restricted to certain systems. In the present case, oxidative polymerization is applied but transition metal-catalyzed alternatives are possible as well. We compare homocoupling-containing and homocoupling-free (semi)crystalline PBTTT-(OR)<sub>2</sub> batches and critically assess common approaches to analyze structural defects. In particular, we emphasize the limitations of MALDI-ToF mass spectrometry in providing a reliable estimate of the type and quantity of specific polymerization errors. We quantify homocoupling defects using STM imaging and confirm the absence of homocoupling for the homopolymerization approach. RHC and T-resolved XRD show that at the fully intercalating molar ratio of polymer and PC<sub>61</sub>BM, no free polymer nor fullerene is present. This further supports

the view that the newly prepared, homocoupling-free polymers have the correct molecular structure to allow for full intercalation and co-crystal formation. Finally, by measuring the EQE for prototype OPDs, we demonstrate that this leads to enhanced direct CT absorption, linked to a higher donor:acceptor interfacial area, and thus inherently allows better device performance. The achieved insights are of a general nature and go beyond the specific PBTTT derivatives studied here. In fact, we demonstrate that, even when the effect of homocoupling defects on the electronic structure is limited, the geometrical effect on polymer crystallinity and/or film morphology can be significant when mixed with a second component and highly relevant for organic electronics, for example, for bulk heterojunction solar cells and photodetectors but also for organic transistors based on molecularly doped polymer semiconductors.

Summarizing, with this work, we intend to raise cognizance that the actual structure of alternating conjugated polymers does not simply correspond to the idealized defect-free picture and that chemical precision can indeed have a profound impact on the final (blend and device) behavior. Ultimately, the actual chemical structures of the constituent molecules will dictate the microstructural, transport, and device properties and a consistent, reproducible structure is crucial for any future application.

## 4. Experimental Section

**MALDI-ToF MS:** Mass spectra were recorded on a Bruker UltrafleXtreme MALDI-ToF/ToF system. Approximately 1 μL of the matrix solution (25 mg mL<sup>-1</sup> *trans*-2-[3-(4-*tert*-butylphenyl)-2-methyl-2-propenyldiene]malononitrile (DTCB) in CHCl<sub>3</sub>) was spotted onto an MTP Anchorchip 600/384 MALDI plate. The spot was allowed to dry and 1 μL of the analyte solution (10 mg mL<sup>-1</sup> in CHCl<sub>3</sub>) was spotted on top of the matrix.

**XPS:** X-ray photoelectron spectroscopy was performed using a PHI VersaProbe 4 with a monochromatized Al Kα source (1486.6 eV, 50 W, 200 μm spot size) and a pass energy of 224 eV. An electron flood gun and low-energy Ar<sup>+</sup> ions were used to neutralize the sample and prevent substrate charging. Binding energies were corrected to the C–C peak in the C 1s signal at 284.8 eV. For all collections, the angle between the sample surface and the detector was 45°. To ensure that the compositions of the measured spectra were representative of the bulk, samples were sputtered with a gas cluster ion beam source (Ar<sub>2000</sub><sup>+</sup>, 10 kV) for 1 min prior to all collections. Atomic concentrations were determined from the peak areas using PHI Multipak software.

**STM:** The experiments were performed under UHV conditions in a low-temperature STM system (CreaTec Fischer & Co. GmbH). The Au(111)/mica substrate (Georg Albert PVD, 300 nm thickness) was cleaned by cycles of Ar<sup>+</sup> ion sputtering (1 × 10<sup>-5</sup> mbar, 10 min) followed by annealing (400 °C, 10 min). The surface was checked by STM for cleanliness before exposure to polymers. Both polymers were dissolved in chlorobenzene at low concentrations (≈0.05 mg mL<sup>-1</sup>). Then, 1.7 mL of the dissolved polymers were mixed with 0.3 mL of methanol, and the mixture was deposited on the gold sample surface under UHV at room temperature by electrospray deposition (Molecularspray Ltd.). The surface was analyzed in situ by STM at a low temperature (−196 °C). All images were acquired in constant current mode and analyzed by WSxM.<sup>[44]</sup> Molecular models of the individual monomers (TT, BT, and T units) and the side chains were first individually optimized in the Avogadro molecular editor using the MMFF94 force field and then superposed onto high-resolution STM images in the LMAPper software.<sup>[45]</sup>

**RHC:** Thermal analysis was performed using rapid heat–cool differential scanning calorimetry by means of a prototype instrument developed by TA instruments.<sup>[46–48]</sup> Calibration of temperature and enthalpy was



performed by using indium standards at 500 K min<sup>-1</sup>. Dedicated aluminum RHC crucibles were filled with samples of around 200–250 µg. Experiments were performed with nitrogen (6 mL min<sup>-1</sup>) as the purge gas.

**X-ray Diffraction/Scattering:** The synchrotron XRD experiments at an X-ray wavelength ( $\lambda$ ) of 1.033 Å were performed at BM26, the scattering dedicated beamline of DUBBLE, the Belgian CRG at the European Synchrotron Radiation Facility (ESRF, Grenoble, France). The XRD patterns were collected in two parts. Scattered intensities at small angles (SAXS) were collected on a Pilatus 1M detector while scattering at wide angles (WAXS) was collected on a Pilatus 300K-W detector. A silver behenate standard was used for the SAXS angular calibration, while silver behenate together with  $\alpha$ -Al<sub>2</sub>O<sub>3</sub> (alumina) was used to calibrate the WAXS. The 2D powder scattering patterns were azimuthally averaged using the ConeX program,<sup>[49]</sup> yielding scattered intensities as a function of the scattering angle, expressed in terms of  $q$ , the modulus of the scattering vector, and related to the scattering angle,  $2\theta$ , via  $q = 4\pi\sin\theta/\lambda$ . With this definition,  $d$ -spacings can be calculated from the  $q$ -position of a given reflection, via  $d = 2\pi/q$ . The WAXS detector was put close to the sample, allowing to cover the range  $0.65 < q < 4 \text{ \AA}^{-1}$ , while the SAXS detector was put at 2 m from the sample, permitting to cover the range  $0.016 < q < 0.5 \text{ \AA}^{-1}$ . The temperature was controlled using a Linkam DSC 600 hot stage. Samples were analyzed in RHC crucibles after having been cooled down at 20 K min<sup>-1</sup> in RHC. These pre-treated samples underwent a heating scan at 50 K min<sup>-1</sup> between 25 and 320 °C while collecting SAXS and WAXS patterns in consecutive 3.4 s time frames, leading to a temperature resolution of 2.83 K.

GIWAXS was performed at the Stanford Synchrotron Radiation Light-source on beamline 11–3, with an X-ray energy of 12.7 keV and an incidence angle of 0.1°. The sample-to-detector distance was 307.5 mm and calibrated to a polycrystalline LaB<sub>6</sub> standard. Measurements were performed in a helium chamber to minimize air scattering. All data was corrected for the geometric distortion of the flat detector used, normalized by exposure time, sample thickness, monitor counts, and analyzed using Nika 1D SAXS<sup>[50]</sup> and WAXStools2 software in Igor Pro.<sup>[51]</sup>

**Theoretical Calculations:** Classical molecular mechanics and molecular dynamics simulations were performed with a modified version of the Dreiding force field, as implemented in the Materials Studio 2018 package. The torsion potentials between adjacent polymer subunits and between the conjugated cores and the alkyl or alkoxy chains were reparameterized and benchmarked against MP2/cc-pVTZ calculations. The atomic charges of the conjugated cores were assigned by fitting the electrostatic potential (ESP charges) calculated at the MP2/6-31G\*\* level on an isolated dimer, while the atomic charges of the alkyl side chains were set to zero. The atomic charges of PC<sub>61</sub>BM were assigned from the COMPASS force field. The electrostatic term was calculated using the Ewald summation method. Before analyzing their dynamical behavior by performing molecular dynamics simulations, the lowest energy structures of all the different systems were determined using a conformational search procedure already reported in detail elsewhere and applied to the benchmark pristine PBTTT system.<sup>[52,53]</sup> When considering PC<sub>61</sub>BM-intercalated systems, a 1:1 monomer:PC<sub>61</sub>BM ratio was chosen. Starting from the lowest energy structures, larger periodic systems containing two layers of four  $\pi$ -stacked hexamers were built and subjected to 500 ps-long equilibration molecular dynamics (NPT;  $p = 1 \text{ atm}$ ) at two different temperatures (25 and 150 °C), followed by a 1 ns-long MD during which the systems were saved every 5 ps and used for further structural analyses. In particular, powder X-ray diffractograms were performed on the 201 structures along the 1 ns MD and the reported interlayer distances correspond to the average interlayer distance of the 201 diffractograms. The reported  $\pi$ - $\pi$  stacking distances were obtained by dividing the average volume of the periodic system by the number of polymer chains, average interlayer distance, and average hexamer length. The as obtained theoretical values were used to confidently assign relevant reflections in the experimental XRD and GIWAXS patterns.

**Device Preparation and Characterization:** The sol-gel ZnO precursor (0.45 M) was prepared by dissolving zinc acetate dihydrate (Aldrich, 99.9%; 0.5 g) and ethanolamine (Aldrich, 99.5%; 0.14 g) in 2-methoxyethanol (Acros Organics, 99.8%; 5 mL). This solution was vig-

orously stirred at 60 °C for 2 h. Stirring was then continued at room temperature overnight in the air to complete the hydrolysis reaction. Solutions of PBTTT-(OR)<sub>2</sub>:PC<sub>61</sub>BM (Solenne) at a total concentration of 25 or 50 mg mL<sup>-1</sup> (20:80 w/w%) were prepared in chloroform/*o*-dichlorobenzene (1.5/1, v/v) and pure *o*-dichlorobenzene for oxidatively polymerized PBTTT-(OR)<sub>2</sub>, and stirred at 70 °C for 5 h in a nitrogen-filled glovebox before use. Standard ITO devices were fabricated using the inverted device structure glass/ITO/ZnO/active layer/MoO<sub>3</sub>/Ag. The ZnO precursor solution was spin-coated on the ITO electrodes at 4000 rpm and annealing was done at 150 °C in air for 20 min to form a 30 nm electron-transporting layer. The prepared samples were then transferred into an N<sub>2</sub>-filled glovebox for spin-coating the active layer (thickness  $\approx 150 \text{ nm}$ ). The blend thickness was monitored by a Bruker Veeco Dektak XT profilometer. Finally, the MoO<sub>3</sub> (10 nm) hole-transporting layer and the Ag (100 nm) top electrode were sequentially deposited on top of the active layer through a shadow mask by thermal evaporation ( $< 5 \times 10^{-6} \text{ mbar}$ ) with an area of 0.06 cm<sup>2</sup>. The EQE<sub>pv</sub> spectrum for each cell was measured under chopped (135 Hz) monochromatic illumination from an Xe lamp (100 W, Newport) modulated by a Cornerstone 130 monochromator and an optical wheel chopper. The generated photocurrent from the solar cells was amplified with a Stanford Research System Model SR830 lock-in amplifier and a calibrated Si photodiode with known spectral response was used as a reference. For the sensitive EQE measurements, an INVENIO R (Bruker Optics) FTIR with quartz beamsplitter and NIR light source was employed. Organic photodiodes were measured using the external detector option of the equipment, in the FTSP configuration.<sup>[28]</sup> A low-noise current amplifier was used to amplify the photocurrent generated under the illumination of the devices, with the illumination light modulated by the Fourier-transform infrared setup.

The OFETs used were bottom-gate bottom-contact where n-doped Si was the gate electrode, 30 nm Au on top of 10 nm ITO was used for the source and drain electrodes, and 90 nm of SiO<sub>2</sub> was applied for the dielectric between the gate and the polymer channel, which had W/L ratios of 500 and 1000 ( $\approx 50/50$  distribution of W/L ratios across all devices).

## Supporting Information

Supporting Information is available from the Wiley Online Library or from the author.

## Acknowledgements

The authors thank the FWO Vlaanderen (Ph.D. and travel grant J.V. (1S50822N and V413722N)), projects G0D0118N and G0B2718N, MALDI-ToF project I006320N, DUBBLE project I001919N, Scientific Research Community “Supramolecular Chemistry and Materials” – W000620N) and the European Research Council (grant 864625) for financial support. J.V. received a personal grant from District 1630 of Rotary International, supported by the Rotary Foundation, allowing a student researcher to visit Stanford University. X.W. acknowledges co-funding from the European Union’s Horizon 2020 research and innovation Marie Skłodowska-Curie Actions, under grant agreement no. 945380. Q.L. acknowledges financial support from the European Union’s Horizon 2020 research and innovation program under the Marie-Curie grant agreement no. 882794. The IMEC and UMONS authors acknowledge funding from the European Commission Horizon 2020 Future and Emerging Technologies project MITICS (964677). D.B. is a FNRS Research Director. T.J.Q. acknowledges support from the National Science Foundation Graduate Research Fellowship Program under grant DGE-1656518. This material is based upon work supported by the U.S. Department of Energy, Office of Science, Office of Workforce Development for Teachers and Scientists, Office of Science Graduate Student Research (SCGSR) program. The SCGSR program is administered by the Oak Ridge Institute for Science and Education for the DOE under contract number DE-SC0014664. Use of the Stanford Synchrotron Radiation Light source, SLAC National Accelerator Laboratory, is supported by the U.S. Department of Energy, Office of Science, Office of Basic Energy Sciences under Contract No. DE-AC02-76SF00515. Part of this work

was performed at the Stanford Nano Shared Facilities (SNSF)/Stanford Nanofabrication Facility (SNF) supported by the National Science Foundation under award ECCS-2026822 and the Stanford SIGMA Facility with support from the Stanford Doerr School of Sustainability.

## Conflict of Interest

The authors declare no conflict of interest.

## Author Contributions

J.V., Z.L., and X.W. contributed equally to this work. J.V. conceived and conceptualized the idea, synthesized and characterized the materials, and performed MALDI-ToF, UV-vis, and GIWAXS data analysis. Z.L. performed the RHC and T-resolved XRD measurements and did the data analysis. X.W. performed the STM experiments and analyzed the resulting data. O.B. was involved in the conceptualization and materials synthesis. S.M. contributed to the analysis of the STM data. T.J.Q. performed the XPS and GIWAXS measurements and helped with data processing. Q.L. did the photodiode measurements. A.G. did the OFET fabrication and analysis. A.M. and K.W. performed the ICP-MS analysis and contributed to the project discussion. M.H. contributed to the T-resolved XRD measurements. B.G. performed and supervised the T-resolved XRD measurements, data analysis, and interpretation in relation to the RHC and simulation data. E.N. contributed to the interpretation of the RHC and XRD data. V.L. performed the simulations. D.B. supervised the simulation work and contributed to the discussions. A.S. supervised the XPS and GIWAXS measurements and contributed to the discussions. L.L. co-supervised the materials synthesis work. K.V. supervised the device work and part of the overall project. B.V.M. contributed to the interpretation of the RHC and T-resolved XRD measurements and co-supervised the project. G.C. supervised the STM experiments and contributed to the discussions. N.V.B. supervised the RHC part of the project and contributed to the discussions. W.M. conceptualized the idea, supervised the materials synthesis and characterization work, and was in charge of the overall project. J.V., B.V.M., and W.M. wrote the manuscript and all authors contributed to the revision and editing.

## Data Availability Statement

The data that support the findings of this study are available from the corresponding author upon reasonable request.

## Keywords

homocoupling, intermolecular charge-transfer absorption, polymer:fullerene co-crystals, Stille cross-coupling, structural defect quantification

Received: August 9, 2023  
Revised: August 24, 2023  
Published online: September 10, 2023

- [1] H. Bronstein, C. B. Nielsen, B. C. Schroeder, I. McCulloch, *Nat. Rev. Chem.* **2020**, *4*, 66.  
[2] G. Hong, X. Gan, C. Leonhardt, Z. Zhang, J. Seibert, J. M. Busch, S. Bräse, *Adv. Mater.* **2021**, *33*, 2005630.  
[3] G. Zhang, F. R. Lin, F. Qi, T. Heumüller, A. Distler, H. J. Egelhaaf, N. Li, P. C. Y. Chow, C. J. Brabec, A. K. Y. Jen, H. L. Yip, *Chem. Rev.* **2022**, *122*, 14180.

- [4] J. Mei, Y. Diao, A. L. Appleton, L. Fang, Z. Bao, *J. Am. Chem. Soc.* **2013**, *135*, 6724.  
[5] H. Ren, J. Chen, Y. Li, J. Tang, *Adv. Sci.* **2021**, *8*, 2002418.  
[6] A. Marks, S. Griggs, N. Gasparini, M. Moser, *Adv. Mater. Interfaces* **2022**, *9*, 2102039.  
[7] H. S. Jung, P. Verwilt, A. Sharma, J. Shin, J. L. Sessler, J. S. Kim, *Chem. Soc. Rev.* **2018**, *47*, 2280.  
[8] J. Kosco, F. Moruzzi, B. Willner, I. McCulloch, *Adv. Energy Mater.* **2020**, *10*, 2001935.  
[9] C. Cordovilla, C. Bartolomé, J. M. Martínez-Illarduya, P. Espinet, *ACS Catal.* **2015**, *5*, 3040.  
[10] N. S. Gobalasingham, B. C. Thompson, *Prog. Polym. Sci.* **2018**, *83*, 135.  
[11] L. Verheyen, P. Leysen, M. P. Van Den Eede, W. Ceunen, T. Hardeman, G. Koeckelberghs, *Polymer* **2017**, *108*, 521.  
[12] K. H. Hendriks, W. Li, G. H. L. Heintges, G. W. P. Van Pruissen, M. M. Wienk, R. A. J. Janssen, *J. Am. Chem. Soc.* **2014**, *136*, 11128.  
[13] F. Lombeck, H. Komber, D. Fazzi, D. Nava, J. Kuhlmann, D. Stegerer, K. Strassel, J. Brandt, A. D. de Zerío Mendaza, C. Müller, W. Thiel, M. Caironi, R. Friend, M. Sommer, *Adv. Energy Mater.* **2016**, *6*, 1601232.  
[14] T. Vangerven, P. Verstappen, J. Drijkoningen, W. Dierckx, S. Himmelberger, A. Salleo, D. Vanderzande, W. Maes, J. V. Manca, *Chem. Mater.* **2015**, *27*, 3726.  
[15] G. Pirotte, P. Verstappen, D. Vanderzande, W. Maes, *Adv. Electron. Mater.* **2018**, *4*, 1700481.  
[16] L. Lu, T. Zheng, T. Xu, D. Zhao, L. Yu, *Chem. Mater.* **2015**, *27*, 537.  
[17] B. Ma, Q. Shi, X. Ma, Y. Li, H. Chen, K. Wen, R. Zhao, F. Zhang, Y. Lin, Z. Wang, H. Huang, *Angew. Chem., Int. Ed.* **2022**, *61*, e202115969.  
[18] J. F. Ponder Jr, H. Chen, A. M. T. Luci, S. Moro, M. Turano, A. L. Hobson, G. S. Collier, L. M. A. Perdigão, M. Moser, W. Zhang, G. Costantini, J. R. Reynolds, I. McCulloch, *ACS Mater. Lett.* **2021**, *3*, 1503.  
[19] D. A. Warr, L. M. A. Perdigão, H. Pinfold, J. Blohm, D. Stringer, A. Leventis, H. Bronstein, A. Troisi, G. Costantini, *Sci. Adv.* **2018**, *4*, eaas9543.  
[20] I. McCulloch, M. Heeney, C. Bailey, K. Genevicius, I. MacDonald, M. Shkunov, D. Sparrowe, S. Tierney, R. Wagner, W. Zhang, M. L. Chabiny, R. J. Kline, M. D. McGehee, M. F. Toney, *Nat. Mater.* **2006**, *5*, 328.  
[21] J. Rivnay, S. C. B. Mannsfeld, C. E. Miller, A. Salleo, M. F. Toney, *Chem. Rev.* **2012**, *112*, 5488.  
[22] M. L. Chabiny, M. F. Toney, R. J. Kline, I. McCulloch, M. Heeney, *J. Am. Chem. Soc.* **2007**, *129*, 3226.  
[23] R. J. Kline, D. M. DeLongchamp, D. A. Fischer, E. K. Lin, L. J. Richter, M. L. Chabiny, M. F. Toney, M. Heeney, I. McCulloch, *Macromolecules* **2007**, *40*, 7960.  
[24] N. C. Miller, E. Cho, R. Gysel, C. Risko, V. Coropceanu, C. E. Miller, S. Sweetnam, A. Sellinger, M. Heeney, I. McCulloch, J. L. Brédas, M. F. Toney, M. D. McGehee, *Adv. Energy Mater.* **2012**, *2*, 1208.  
[25] A. C. Mayer, M. F. Toney, S. R. Scully, J. Rivnay, C. J. Brabec, M. Scharber, M. Koppe, M. Heeney, I. McCulloch, M. D. McGehee, *Adv. Funct. Mater.* **2009**, *19*, 1173.  
[26] E. Buchaca-Domingo, K. Vandewal, Z. Fei, S. E. Watkins, F. H. Scholes, J. H. Bannock, J. C. de Mello, L. J. Richter, D. M. DeLongchamp, A. Amassian, M. Heeney, A. Salleo, N. Stingelin, *J. Am. Chem. Soc.* **2015**, *137*, 5256.  
[27] T. M. Burke, S. Sweetnam, K. Vandewal, M. D. McGehee, *Adv. Energy Mater.* **2015**, *5*, 1500123.  
[28] K. Vandewal, K. Tvingstedt, A. Gadisa, O. Inganäs, J. V. Manca, *Nat. Mater.* **2009**, *8*, 904.  
[29] Z. Tang, Z. Ma, A. Sánchez-Díaz, S. Ullbrich, Y. Liu, B. Siegmund, A. Mischok, K. Leo, M. Campoy-Quiles, W. Li, K. Vandewal, *Adv. Mater.* **2017**, *29*, 1702184.

- [30] C. Kaiser, K. S. Schellhammer, J. Benduhn, B. Siegmund, M. Tropiano, J. Kublitski, D. Spoltore, M. Panhans, O. Zeika, F. Ortmann, P. Meredith, A. Armin, K. Vandewal, *Chem. Mater.* **2019**, *31*, 9325.
- [31] J. Vanderspikken, Q. Liu, Z. Liu, T. Vandermeeren, T. Cardeynaels, S. Gielen, B. Van Mele, N. Van den Brande, B. Champagne, K. Vandewal, W. Maes, *Adv. Funct. Mater.* **2021**, *32*, 2108146.
- [32] F. C. Jamieson, E. B. Domingo, T. McCarthy-Ward, M. Heaney, N. Stingelin, J. R. Durrant, *Chem. Sci.* **2012**, *3*, 485.
- [33] M. A. Ansari, S. Mohiuddin, F. Kandemirli, M. I. Malik, *RSC Adv.* **2018**, *8*, 8319.
- [34] B. S. Ong, Y. Wu, P. Liu, S. Gardner, *J. Am. Chem. Soc.* **2004**, *126*, 3378.
- [35] H. Pan, Y. Li, Y. Wu, P. Liu, B. S. Ong, S. Zhu, G. Xu, *J. Am. Chem. Soc.* **2007**, *129*, 4112.
- [36] A. L. Jones, M. De Keersmaecker, I. Pelse, J. R. Reynolds, *Macromolecules* **2020**, *53*, 7253.
- [37] P. Verstappen, J. Kesters, W. Vanormelingen, G. H. L. Heintges, J. Drijkoningen, T. Vangerven, L. Marin, S. Koudjina, B. Champagne, J. Manca, L. Lutsen, D. Vanderzande, W. Maes, *J. Mater. Chem. A* **2015**, *3*, 2960.
- [38] R. K. Hallani, B. D. Paulsen, A. J. Petty, R. Sheelamantula, M. Moser, K. J. Thorley, W. Sohn, R. B. Rashid, A. Savva, S. Moro, J. P. Parker, O. Drury, M. Alsufyani, M. Neophytou, J. Kosco, S. Inal, G. Costantini, J. Rivnay, I. McCulloch, *J. Am. Chem. Soc.* **2021**, *143*, 11007.
- [39] S. Moro, N. Siemons, O. Drury, D. A. Warr, T. A. Moriarty, L. M. A. Perdigão, D. Pearce, M. Moser, R. K. Hallani, J. Parker, I. McCulloch, J. M. Frost, J. Nelson, G. Costantini, *ACS Nano* **2022**, *16*, 21303.
- [40] I. E. Jacobs, Y. Lin, Y. Huang, X. Ren, D. Simatos, C. Chen, D. Tjhe, M. Statz, L. Lai, P. A. Finn, W. G. Neal, G. D'Avino, V. Lemaury, S. Fratini, D. Beljonne, J. Strzalka, C. B. Nielsen, S. Barlow, S. R. Marder, I. McCulloch, H. Sirringhaus, *Adv. Mater.* **2022**, *34*, 2102988.
- [41] E. Cho, C. Risko, D. Kim, R. Gysel, N. C. Miller, D. W. Breiby, M. D. McGehee, M. F. Toney, R. J. Kline, J. L. Brédas, *J. Am. Chem. Soc.* **2012**, *134*, 6177.
- [42] Z. Peng, N. Stingelin, H. Ade, J. J. Michels, *Nat. Rev. Mater.* **2023**, *8*, 439.
- [43] Z. Li, Q. Shi, X. Ma, Y. Li, K. Wen, L. Qin, H. Chen, W. Huang, F. Zhang, Y. Lin, T. J. Marks, H. Huang, *Nat. Commun.* **2023**, *13*, 144.
- [44] I. Horcas, R. Fernández, J. M. Gómez-Rodríguez, J. Colchero, J. Gómez-Herrero, A. M. Baro, *Rev. Sci. Instrum.* **2007**, *78*, 013705.
- [45] L. M. A. Perdigão, LMAPper – The SPM and Mol Viewer Reviews, SourceForge.net.
- [46] R. L. Danley, P. A. Caulfield, S. R. Aubuchon, *Am. Lab.* **2008**, *41*, 9.
- [47] S. Wouters, F. Demir, L. Beenaerts, G. Van Assche, *Thermochim. Acta* **2012**, *530*, 64.
- [48] M. Defour, N. Van Den Brande, L. Van Lokeren, G. Van Assche, W. Maes, D. Vanderzande, B. Van Mele, *RSC Adv.* **2016**, *6*, 92981.
- [49] C. J. Gommers, B. Goderis, *J. Appl. Crystallogr.* **2010**, *43*, 352.
- [50] J. Ilavsky, *J. Appl. Crystallogr.* **2012**, *45*, 324.
- [51] S. D. Oosterhout, V. Savikhin, J. Zhang, Y. Zhang, M. A. Burgers, S. R. Marder, G. C. Bazan, M. F. Toney, *Chem. Mater.* **2017**, *29*, 3062.
- [52] V. Lemaury, L. Muccioli, C. Zannoni, D. Beljonne, R. Lazzaroni, J. Cornil, Y. Olivier, *Macromolecules* **2013**, *46*, 8171.
- [53] V. Lemaury, J. Cornil, R. Lazzaroni, H. Sirringhaus, D. Beljonne, Y. Olivier, *Chem. Mater.* **2019**, *31*, 6889.